Regulating the Front-line Orbital Energy Level Enables High-Rate Performance for Lithium-Sulfur Containing Polymers Batteries

Rong Zou[1,2], Wenwu Liu[1], Binhang Zhao[2], Jie Zhang[1], Lei Zhao[1], Xuejun Ren[3*], Haifei Zhang[2*], Fen Ran[1*]

[1] *Energy Storage Institute of Lanzhou University of Technology, State Key Laboratory of Advanced Processing and Recycling of Non-ferrous Metals, Department of Polymeric Materials Engineering, School of Materials Science and Engineering, Lanzhou University of Technology, Lanzhou 730050, Gansu, China*

[2] *Department of Chemistry, University of Liverpool, Oxford Street, Liverpool L69 7ZD, UK*

[3] *School of Engineering, Liverpool John Moores University, Byrom Street, Liverpool, L3 3AF UK*

*Corresponding Authors: Dr. Prof. Fen Ran, ranfen@lut.edu.cn or ranfen@163.com, Dr. Haifei Zhang, zhanghf@liverpool.ac.uk; and Prof. Xuejun Ren, x.j.ren@ljmu.ac.uk.

Abstract: Sulfur-containing polymers are promising cathode materials for lithium batteries, offering a novel pathway toward high-energy batteries. Moreover, tuning the frontier orbital energy levels of sulfur-containing polymers can accelerate electrochemical reaction kinetics. Herein, an organic cathode material containing selenium is synthesized using a selenium sulfide solid solution via a previously proposed thiol-sulfur click chemistry reaction, which is a rubber-like material with good mechanical properties. According to front-line orbital theory, the introduction of selenium a group VI element like sulfur, leads to sp^3 hybridization and sulfur–Selenium covalent bond formation. Owing to the electronegativity disparity between sulfur and selenium, electrons accumulate near sulfur atoms, creating nucleophilic sites and continuous negative regions that promote Li^+ transport. As a result, the Li^+ diffusion coefficient increases from 9.7×10^{-13} cm^2 S^{-1} to 2.7×10^{-12} cm^2 S^{-1}. The bandgap narrows from 4.14 to 3.89 eV, facilitating lithiation process and enhancing electrochemical performance. Among the cathode materials with different selenium content, the fabricated materials exhibit a superior initial capacity of 580 mAh g^{-1} at 0.05 C and well longer cycle stability. This study reveals how doping modulates frontier orbital energy levels can be employed to enhance reaction kinetics, offering insights for improving sulfur containing polymers-lithium batteries performance.

Key Words: Thiol-Sulfur Click Chemistry; Frontier Orbital Theory; Se-doped; Reaction Kinetics; Lithium-Sulfur containing polymers Batteries.

1. Introduction

Organic electrode materials (OEMs) have recently emerged as competitive alternatives to conventional inorganic electrode materials[1]. Various OEMs exhibit distinct advantages. Conjugated polymers possess excellent electronic conductivity and can prepare high mass loaded electrodes, though their cycling stability remains unsatisfactory. In contrast, quinone-based OEMs offer superior stability and high specific capacities. Representative examples include anthraquinone (AQ, 256 mAh g^{-1})[2], benzoquinone (BQ, 496 mAh g^{-1})[3], and phenanthrenequinone (PQ, 256 mAh g^{-1})[4], as well as polymeric derivatives of quinones such as poly(2-chloro-3, 5, 6-trisulfide-1, 4-benzoquinone) (PCTB, 343.1 mAh g^{-1})[5], poly(benzoquinonyl sulfide) (PHBQS, 388 mAh g^{-1})[6], and anthraquinone-phenylamine CMPs (TNAQ, 236 mAh g^{-1})[7]. It has been revealed that sulfur-containing OEMs tend to deliver significantly enhanced specific capacities from insight into molecular-level structural engineering. Sulfur-containing polymer (SCP) electrode materials, owing to their relatively high sulfur content, a sustainable, non-metallic element, can not only modulate redox potentials but also provide high energy densities. Furthermore, their unique molecular flexibility, multifunctionality, low cost, and environmental friendliness, along with the ability to accommodate the structural stress arising during redox reactions, make them promising candidates for metal-ion batteries (MIBs), delivering outstanding electrochemical performance[8].

Prior studies have shown that although SCPs offer multiple advantages[9-11]. For example, the flexible polymer chains segments can accommodate the structural changes arising from the volumetric expansion/constriction during redox reaction, thereby preventing electrode collapse. SCP-based lithium (SCP-Li) batteries still face two major challenges: the generation of lithium polysulfides (LiPSs), which leads to the shuttle effect; and sluggish reaction kinetics, resulting in non-ideal rate performance. To address the shuttle effect, structural design of SCPs can be employed by exploiting the tunable nature of their molecular frameworks[12]. Electron-donating functional groups can be introduced at appropriate sites to adsorb LiPSs. In prior study, with acid-doped polyaniline backbones, a reversible transition occurs between protonated and deprotonated quinonoid imine states during charging/discharging processes. The lone pair (L.p) on the deprotonated quinonoid-N can couple with terminal Li on LiPSs, that effectively anchoring LiPSs and suppressing the shuttle effect[13]. In general, controlling the number of sulfur atoms in the sulfur chains to fewer than six ($-S_x-$, $2 < x \leq 6$) can significantly reduce shuttling[10, 14]. To accelerate the battery reaction kinetics, heteroatom doping can be introduced to facilitate lithiation reactions[15]. This not only enhances redox potential but also improves the electronic conductivity of the material, increasing the carrier mobility and thereby delivering superior electrochemical performance. Iodine doping in the conductive polymer polyacetylene (PA) increases the redox potential to 3.95 V (vs. Li/Li^+), while improving electrical conductivity by approximately ten orders of magnitude[16]. Similarly, a composite cathode material (MoS_2-NG@S-SH) has been developed by in situ integration of MoS_2-modified N-doped graphene (MoS_2-NG) with an organic sulfide active material (S–SH). This architecture enhances both the density of adsorption sites and catalytic sites, lowers the energy barrier for LiPSs conversion, and thus promotes faster reaction kinetics[17].

In this work, a thiol-sulfur click chemistry[18], proposed in prior work, is employed to synthesize SCP with short sulfur-chains by fine-tuning the stoichiometric ratio of the reactants. The method is simple and easy to operate. First, infinite solid solution of SSe is prepared, and then reacted with 2, 2'-thiodiethanethiol (TDET) under ambient conditions using diethylamine as a catalyst, yielding polydivinylthio-selenide (PDVTSSe). A sp^3 hybridization occurs between S and Se forming both (S–Se) bond and (S–Se)* anti-bond. The incorporation of selenium modulates the density of states of the sulfur sp^3 orbitals, bringing the Fermi level (E_f) closer to the sp^3 orbital center. The highest occupied molecular orbital (HOMO) shifts upward toward the lowest unoccupied molecular orbital (LUMO), thereby narrowing the bandgap. Terminal lithium ions with 1*s* vacant orbitals overlap with the fully occupied sulfur sp^3 orbitals, forming stable Li–S bonds. Density functional theory (DFT) calculations reveal that the bandgap of PDVTHS decreases from 4.14 eV to 3.89 eV in $PDVTSSe_{0.325}$, making the lithiation reaction thermodynamically more favorable. Galvanostatic intermittent titration technique (GITT) and rate performance tests clearly demonstrate that the introduction of Se increases the Li^+ diffusion coefficient by an order of magnitude, reaching 2.7×10^{-12} cm^2 S^{-1}. Additionally, the material retains a high discharging capacity of 210 mAh g^{-1} even at a high current rate of 2 C. This study employs frontier orbital energy level engineering to introduce the heteroatom Se, thereby enhancing the reaction kinetics of the battery. Furthermore, Se-doped SCPs are directly synthesized via thiol-sulfur click chemistry, providing a novel strategy for the rational design of organic cathode materials.

2. Experimental

2.1 Materials and Chemicals

Sulfur (S_8, ≥ 99.5 %, *Canrd*), Selenium (Se, *Aladdin*), 2, 2'-thiodiethanethiol (TDET, $C_4H_{10}S_3$, > 97 % (GC), *Macklin*), CNT paper (*Nanotechlab*), Li-S battery electrolyte (LiTFSI, *Canrd*), Celgard 2500 as the separator (*Canrd*) were purchased and used as received. Methylbenzene (PhMe) carbon, disulfide (CS_2), and diethylamine (Et_2NH) were purchased from *Chemical Reagents Co. Ltd., China*. All the reagents were analytical grade and used as received.

2.2 Synthesis of SeS Solid Solution

Selenium and sulfur powders (commercially available) were ground together at weight ratios of 1: 3, 1: 6, and 1: 15. The mixtures were transferred into 20 mL hydrothermal reactors and heated at 250 °C for 24 h. Upon cooling to room temperature, a series of SeS solid solutions were obtained, and referred to as SeS-3, SeS-6 and SeS-15, respectively.

2.3 Synthesis of PDVTSSe and PDVTHS

The synthesis was carried out in an argon-filled glovebox (H_2O and O_2 < 1 ppm, Mikrouna). SeS and TDET were added to a $MePh/CS_2$ mixture (V/V = 1: 1) at a molar ratio of 5: 1, followed by vigorous stirring until complete dissolution. Subsequently, 5 μL of catalytic Et_2NH was introduced into the solution, resulting in immediate effervescence of H_2S gas, which subsided within 10 minutes. The resulting solution was promptly injected into CNT paper to prepare the cathode. The rest of the resulting solution was stirred overnight to yield the sulfur-containing polymer PDVTHS as a precipitate. The final product was dried in an oven at 60 °C for subsequent characterization. The synthesis of PDVTHS followed the same procedure as that of PDVTSSe, except using S_8 in place of the SeS solid solution.

2.4 Synthesis of PDVTSSe/PDVTHS Cathode

CNT paper was punched into 12 mm diameter discs and dried in a vacuum oven for 12 h. Subsequently, 20 μL of the PDVTSSe/PDVTHS solution was drop-cast onto the CNT discs (typically containing 0.01 mmol or 2.8 mg of active material). The in-situ solidification of PDVTSSe/PDVTHS proceeded upon slow evaporation of CS_2, leading to gradual precipitation of the SCP within the CNT framework. The resulting cathode exhibited an aerial loading of 2.47 mg cm^{-2}. All procedures were conducted in an argon-filled glovebox.

2.5 Materials Characterization

The microstructure of the PDVTSSe/PDVTHS cathode was examined using field-emission scanning electron microscopy (FE-SEM, JSM-6701F, JEOL, Japan). Elemental distribution was analyzed by energy-dispersive X-ray spectroscopy (EDS) mapping (Gemini 300, Zeiss). The elemental composition (S and Se) was determined by inductively coupled plasma-optical emission spectrometer (ICP-OES). X-ray diffraction (XRD) patterns were recorded using a Bruker D8 ADVANCE diffractometer with Cu Kα radiation (λ = 0.1541 nm). Fourier-transform infrared (FTIR) spectra were collected in the range of 4, 000~600 cm^{-1} using a Vectory-80 spectrometer (Bruker, Germany). Raman spectra of the SeS solid solution, pure S and, Se powder were measured over the range of 100–600 cm^{-1} using a HORIBA XploRA Plus Raman spectrometer (China). ST2643 high-resistance meter was used to assess electronic conductivity of a series SeS solid solution powder, S and Se. X-ray photoelectron spectroscopy (XPS, ESCALAB 250Xi, Thermo Fisher Scientific) was employed to analyze the chemical states of the SeS solid solution, PDVTSSe/PDVTHS polymer and the corresponding cathodes, with calibration based on the C 1*s* peak at 284.8 eV. Thermogravimetric analysis (TGA, Discovery TGA, TA Instruments) was performed from 25 °C to 800 °C at a heating rate of 10 °C min^{-1} under an argon atmosphere.

2.6 Electrochemical Measurements

CR2032-type coin cells were assembled in an argon-filled glovebox. The cathode was paired with a lithium metal anode, with a Celgard 2500 membrane serving as the separator. A total of 20 μL of commercial Li-S electrolyte was added to both sides of the separator. The cells were sealed and electrochemical measurements were performed. Cyclic voltammetry (CV) was conducted using an electrochemical workstation (CHI760E, Shanghai, China) in the voltage range of 1.6~3.0 V at a scan rate of 0.1~0.5 mV s^{-1}. Electrochemical impedance spectroscopy (EIS) was also performed on the same workstation to evaluate changes in charge-transfer resistance (R_{ct}) before and after cycling, over a frequency range of 100 kHz to 0.01 Hz. Galvanostatic charge/discharge (GCD) tests, rate performance, and cycling stability were measured using a battery testing system (CT2001A, LAND, Wuhan, China) within a voltage window of 1.6–3.0 V. GITT tests were performed at a current density of 0.1 C for 10 min and relaxation for 10 min. The specific capacity was calculated based on a theoretical value of 920.3 mA g^{-1} (1 C rate).

2.7 Calculation Methods

DFT calculations were performed using the ORCA 6.0.1 software package [19]. Geometry optimizations for both ground and transition states were conducted with hybrid-GGA functional B3LYP and split valence def2-SVP basis set[20]. Grimme's dispersion correction DFT-D3(BJ) method was applied for optimization. The local minima structures were confirmed by vibrational frequencies with zero imaginary frequency. The Shermo package was used to derive the thermodynamic correction terms for the computed structures[21]. The 3D structures were visualized with VESTA.

The first principle calculations (periodicity structures) were carried out with the CP2K 2025.1 software package with Perdew-Burke-Ernzerhof (PBE) functional and Grimme's DFT-D3(BJ) van der Waals correction method, during which the DZVP-MOLOPT-SR-GTH basis set and Goedecker-Teter-Hutter (GTH) pseudopotential were employed[22]. The plane-waves were cut off at 400 Ry. The ESP figures were rendered by means of the VMD visualization program[23].

3. Results and Discussion

In our previous study[18], the organic cathode material PDVTHS has been synthesized using thiol-sulfur click chemistry, which has high specific capacity and excellent cycling stability in SCP-Li sulfur batteries. To further enhance the reaction kinetics of the cathode and improve battery performance, selenium (Se) doping is introduced. In this work, three PDVTSSe materials with varying Se content as cathode active materials are prepared. According to the phase diagram, S and Se can form infinite solid solutions. By adjusting the S/Se molar ratio, three solid solutions: SeS-15, SeS-6, and SeS-3, with increasing Se content were synthesized. As shown in Figure 1a), the Se concentration increases the material color deepened, approaching that of pure Se. Figure 1b) presents the electrical conductivity measurements, revealing that pure Se exhibited the highest conductivity, whereas pure S shows the lowest. The electrical conductivity of the SeS solid solutions increase systematically with increasing Se content. Figure 1c) shows X-ray diffraction (XRD) patterns of SeS-15, SeS-6, SeS-3, pure S and Se showed distinct peaks at 24° and 24.6°, corresponding to the SeS solid solution phase[24]. These peaks differed from those of pure S and Se, and the characteristic peaks of S and Se become weaker, confirming the formation of a new solid solution phase with a crystal structure distinct from either pure S or Se. Raman spectra further confirm these findings (Figure 1d)). A new peak appears at approximately 380 cm^{-1}, attributed to the SeS solid solution phase. The peaks observed at 153, 218.3, and 472 cm^{-1} are attributed to symmetric vibrations of S–S bond, and that at 218.3 cm^{-1} corresponding to the deformation of S–S bonds within the SeS solid solution. Additionally, a new peak at 380 cm^{-1} is detected in the SeS solid solution, which is assigned to the vibrational of Se–S bond[25]. The Se–S bond signal is more intense in SeS-3 than that in SeS-15, indicating a higher degree of Se substitution in samples with greater Se content. This substitution leads to the formation of more Se–S bond. Furthermore, a blue shift of the peaks from 478 to 371 cm^{-1} can be attributed to ring deformation caused by the incorporation of Se atoms into the S_8 ring structure[26].

Due to S has a higher electronegativity than Se, the formation of the SeS solid solution causes electron transfer along the atomic chain toward the S atoms adjacent to Se–S bonds. This results in an increased electron cloud density around S atoms. Correspondingly, X-ray photoelectron spectroscopy (XPS) reveals a negative shift in the S 2*p* peak. Meanwhile, the Se 3*p* peak exhibits a positive shift, owing to the reduced electron density around Se. As shown in Figure 1e), the fitted S 2*p* and Se 3*p* spectra of the SeS-6 sample display peaks at 164 and 162.8 eV assigned to S 2*p*, and peaks at 166.7 and 161.1 eV assigned to Se 3*p*[24]. The partial overlap between the S 2*p* and Se 3*p* peaks reflects the interaction between Se and S via Se–S bonding. Compared to the binding energies of S 2*p* in pure S (164.4 and 163.3 eV), the S 2*p* peaks in SeS-6 shift negatively by 0.4 and 0.5 eV, respectively. Similarly, relative to Se 3*p* peaks in pure Se (166.4 and 160.7 eV), those in SeS-6 shift positively by approximately 0.3 eV. These shifts indicate partial reduction of S and partial oxidation of Se within the SeS solid solution, confirming interaction between Se and S atoms.

According to our previously reported thiol–sulfur click chemistry[18], polydivinylthio-selenide (PDVTSSe) was synthesized via the reaction of 2,2'-thiodiethanethiol (TDET) with SeS solid solutions at room temperature, using diethylamine ($(Et)_2NH_2$) as the catalyst, as illustrated in Figure S1 in Supplementary Information. The color change during the synthesis could be clearly observed in glass vials. As the Se content increases, the color of the solution gradually deepened, with the SeS-3 sample exhibiting the darkest appearance. The resulting liquid PDVTSSe is quickly drop-cast onto carbon nanotube (CNT) paper (20 μL per piece, 22.48 mg cm^{-2} of mass load). The remaining solution was transferred to a 60 °C oven and dried overnight. After solvent evaporation, PDVTSSe formed a brownish rubber-like solid with a certain degree of flexibility. The S and Se contents in different SCP materials are determined by inductively coupled plasma optical emission spectroscopy (ICP-OES), and the detailed results are summarized in **Table S1** in Supplementary Information. The synthesized PDVTSSe with various Se content are recorded as $PDVTSSe_{0.191}$, $PDVTSSe_{0.325}$, $PDVTSSe_{0.776}$. In the sample $PDVTSSe_{0.191}$, the S content was 70.05 %, and the Se content was 4.73 %, corresponding to an atomic ratio of S to Se of approximately 1:0.03. For $PDVTSSe_{0.325}$, the S and Se contents were 68.66 % and 7.87 %, respectively, with an atomic ratio of 1: 0.05. In $PDVTSSe_{0.776}$, the S content was 63.22 %, and the Se content increased to 17.3 %, yielding an atomic ratio of 1: 0.11. X-ray diffraction (XRD) analysis is performed on $PDVTSSe_{0.191}$, $PDVTSSe_{0.325}$, and $PDVTSSe_{0.776}$ with varying selenium contents, and the results are compared with those of non-selenized PDVTHS, as well as with pure S and Se powders (Figure 2a). No characteristic peaks of elemental sulfur were observed in PDVTHS, indicating that sulfur was fully incorporated into the polymer chains through chemical bonding. The broad diffraction peak observed in the low-angle region (10°~20°) is attributed to the scattering of amorphous materials, confirming the polymeric nature of the product. Similarly, the XRD patterns of $PDVTSSe_{0.191}$, $PDVTSSe_{0.325}$, and $PDVTSSe_{0.776}$ also exhibit broad shape, featureless diffraction signals without distinct S or Se crystalline peaks, further indicating their amorphous nature and the complete incorporation of S and Se into the polymer backbone. The XPS analysis of survey spectrum on $PDVTSSe_{0.325}$ is shown in Figure 2b), the sample contains C, S and, Se. Figure 2c) deliveries the fine spectrum of C 1*s*, S 2*p* and, Se 3*d*. C 1*s* exhibits a peak at 284.2 eV, which is attributed to C–S bonds. The S 2*p* spectrum displays two peaks at 164.0 and 162.8 eV, corresponding to the S $2p_{1/2}$ and S $2p_{3/2}$ components, respectively. These peaks are associated with S–S, S–Se and, S–C bonds. The fine Se 3*d* spectrum shows peaks at 55.9 and 55.0 eV, which can be assigned to Se–S bonding. These peaks are positively shifted by 2.7 eV compared to the Se–Se peaks in pure elemental Se (53.2 and 52.3 eV, Figure S2 in Supplementary Information), indicating that Se is chemically bonded to S in the polymer chain and is partially oxidized by the surrounding S atoms[27].

The XRD pattern of PDVTSSe (Figure 2d)) reveals no crystalline peaks associated with elemental S, Se, or SeS solid solution, suggesting that the reaction proceeded to completion with full conversion into the polymeric product. The only visible peak at 26° originates from the CNT paper substrate, consistent with the XRD pattern of pristine CNT paper (Figure S3 in Supplementary Information). Figure 2e) expresses Fourier-transform infrared (FTIR) spectroscopy that further confirms the transformation of the precursor TDET into the PDVTSSe polymer. The S–H characteristic stretching vibration at 2546 cm^{-1} observed in TDET disappears after polymerization, while a new peak at 833.5 cm^{-1} emerges, indicating S–S bond formation and successful crosslinking. In addition, the vibrations at 713.5 cm^{-1} (C–S bond) and 1, 415.5 cm^{-1} (C–H bond) are significantly weakened compared to those in TDET, which may result from a reduction in molecular freedom upon polymerization. In addition, doping contributes to improved thermal robustness of the material (Figure S4 in Supplementary

Information).

As shown in Figure 2f), the PDVTSSe synthesized via thiol–sulfur electrochemical click chemistry, exhibits a rubber-like texture with inherent mechanical flexibility. A $PDVTSSe_{0.325}$ strip measuring 4 cm in length could be stretched to 6.5 cm and be capable of lifting a 500 g weight with ease, demonstrating its mechanical robustness. To quantitatively evaluate its mechanical properties, Figure 2g) compares the toughness and Young's modulus of samples with varying Se content, including the Se-free PDVTHS. Se incorporation is found to enhance both the stiffness and toughness of the polymer network. The incorporation of Se atoms likely introduces interfacial reinforcement, effectively restricting chain segment mobility and enhancing the bulk mechanical properties. Moreover, Se may modulate the electronic structure or charge distribution, thereby strengthen intermolecular interactions and further improving mechanical robustness[28-30]. Specifically, the Se-free PDVTHS exhibit a Young's modulus of 282 kPa and a toughness of 0.087 MJ m^{-3}, reflecting low rigidity. Upon Se doping, both Young's modulus and toughness increase significantly, $PDVTSSe_{0.191}$ (289 kPa, 0.181 MJ m^{-3}), $PDVTSSe_{0.325}$ (513 kPa, 0.489 MJ m^{-3}), $PDVTSSe_{0.776}$ (407 kPa, 0.365 MJ m^{-3}). Young's modulus reflects a material's resistance to elastic deformation. A higher value indicates greater stiffness. Toughness quantifies the energy a material can absorb before fracturing. In the context of battery electrodes, increased toughness allows the material to accommodate volume changes caused by redox reactions of the active species, helping to prevent cathode structural collapse. Interestingly, both Young's modulus and toughness exhibit a non-monotonic trend with increasing Se content: they first increase and then decrease, reaching their peak values in $PDVTSSe_{0.325}$. This suggests that moderate Se doping substantially improves mechanical performance, while excessive Se content may compromise the polymer's structural integrity. Therefore, optimizing Se concentration is critical for balancing elasticity and strength in polymer-based cathodes.

Figure 2h) shows the stress-strain curves, both stress and strain values is improved with Se incorporation. For PDVTHS, the tensile stress and strain were 0.142 MPa and 0.937%, respectively. These values increased in $PDVTSSe_{0.191}$ (0.175 MPa, 1.43%) and $PDVTSSe_{0.776}$ (0.38 MPa, 1.43%), reaching the highest levels in $PDVTSSe_{0.325}$ (0.41 MPa, 1.60%). This indicates that $PDVTSSe_{0.325}$ possesses the best tensile performance among the tested samples. To enhance the electrical conductivity of the cathode, active materials with different Se contents is loaded onto CNT paper to fabricate PDVTSSe composite electrodes, hereafter referred to as $PDVTSSe_{0.191}$, $PDVTSSe_{0.325}$, and $PDVTSSe_{0.776}$. The scanning electron microscopy (SEM) images of these electrodes are shown in Figure S5 in Supplementary Information. Despite the varying Se content, no significant morphological differences are observed among the three samples. Compared with pristine CNT paper (Figure S6 in Supplementary Information), the SEM images clearly reveal that the polymer coats the CNT network uniformly. EDS mapping further confirms the homogeneous distribution of C, S, and Se on the electrode surface.

Figure 3 presents the galvanostatic intermittent titration technique (GITT) curves of SCP electrodes with three different selenium contents. All electrodes exhibit similar electrochemical behavior and charging/discharging plateaus. Compared to the PDVTHS cathode, which shows an average voltage plateau of 2.08 V (Figure S7 in Supplementary Information), the average plateau increases to approximately 2.14 V for the Se-containing cathodes. This increase is attributed to the inherent redox potential of S/S^{2-} in the SSe solid solution (0.142 V vs. SHE), which is higher than the redox potential of Se/Se^{2-} in pure selenium (-0.399 V vs. SHE). As shown in Figure 3a-c) the Se content increases, the average polarization voltage between transient curves (solid lines) decreases, indicating reduced electrochemical polarization of the batteries. Additionally, the polarization voltages between the steady-state curves (dashed circles) are 0.185 V, 0.149 V, and 0.14 V for PDVTSSe0.191, PDVTSSe0.325, and PDVTSSe0.776 cathodes, respectively. This reduction in polarization is not only due to improved polymer conductivity from Se doping but also confirms the synergistic effect between S and Se within the SCP. Measurement of the lithium ions diffusion coefficient is a crucial method for investigating electrode kinetics. A higher diffusion coefficient corresponds to better high-current discharge capability, higher power density, and improved rate performance of the electrode material. Inhere, GITT is employed to estimate the lithium-ion diffusion coefficient (D_{Li+}) within the active material. By analyzing the relationship between the electrode potential changes and the relaxation time, combined with the physicochemical parameters of the active material, the impact of selenium doping in the SCP on the battery reaction kinetics is evaluated. The Li^+ diffusion coefficient is calculated according to the following equation[31]:

$$D = \frac{4}{\pi\tau}\left(\frac{m_b V_m}{M_b S}\right)^2 \left(\frac{\Delta E_s}{\Delta E_t}\right)^2$$

where τ is the relaxation time; m_b is the mass of the active material; V_m is the molar volume of the electrode material; M_b is the molar mass of the active material; S is the electrode/electrolyte contact area; ΔE_s is the voltage change caused by the current pulse; and ΔE_t is the voltage change during the constant current charge (discharging).

As demonstrated in Figures 3a-c), the GITT curves of cathodes with different Se contents, exhibiting similar voltage plateaus and electrochemical behaviors. Consistent with previous reports, the high-voltage plateau at a depth of discharge of around 18 % corresponds to the cleavage of C–S bonds in PDVTSSe. These C−S bonds have lower bond energy than S–S and S–Se bonds. During this stage, two Li^+ ions combine to form $LiS_2C_4H_8S_2SeLi$, resulting in a faster Li^+ diffusion rate, reaching up to 10^{-10} cm^2 S^{-1} (Figure 3d and f)) and even 10^{-9} cm^2 S^{-1} in $PDVTSSe_{0.325}$ (Figure 3e)). At a depth of discharge between 18 % and 90 %, the Li^+ diffusion coefficients are significantly improved compared to the PDVTHS cathode (Figure S7 in Supplementary Information), and the diffusion curves are more stable. The values are 5.3×10^{-13} cm^2 S^{-1}, 2.7×10^{-12} cm^2 S^{-1}, and 7.4×10^{-12} cm^2 S^{-1} for $PDVTSSe_{0.191}$, $PDVTSSe_{0.325}$, and $PDVTSSe_{0.776}$ cathodes, respectively. This plateau corresponds to the further discharging of intermediate products to the final discharge products, including 2, 2'-thiobis(lithium ethithiolate) ($LiSC_4H_8S_2Li$), Li_2S, and Li_2Se. During the charging plateau, the Li^+ diffusion coefficient in the $PDVTSSe_{0.325}$ electrode shows a more pronounced increase, reaching 5.0×10^{-11} cm^2 S^{-1} at 60 % state of charge. The charging plateau represents the reversible conversion of discharging products back to the reactant PDVTSSe. The enhanced Li^+ diffusion rate can be attributed partly to the improved electrical conductivity of the active material and partly to the presence of Se, which facilitates electron fast transfer. Consequently, this superior conductivity promotes the easier interconversion between high-order polysulfides, low-order polysulfides, and discharge products.

To investigate the impact of Se doping on the electrode kinetics, cyclic voltammetry (CV) tests are performed on the three cathodes at scan rates ranging from 0.1 to 0.5 mV s^{-1} (Figure 4a-c)). The CV curves maintain consistent shapes across different scan rates, demonstrating excellent electrochemical stability. With increasing Se content, the electrochemical polarization of the electrodes exhibits a trend of initially decreasing followed by increasing illustrated in Figure S8 in Supplementary Information. Among them, the PDVTSSe0.325 cathode shows the lowest polarization of 0.37 V. Since larger polarizatioSn hinders rapid reaction kinetics, this observation is consistent with the GITT-derived kinetic profiles, where PDVTSSe0.325 exhibits the highest Li^+ diffusion coefficient. Further analysis of the oxidation peak A and reduction peaks B and C allowed plotting of peak current (Ip) versus the square root of scan rate (v0.5) curves in Figure 4d-f). Although PDVTSSe0.776 and PDVTSSe0.191 showed larger slopes in reduction peak B, likely due to faster electrochemical conversion at the first plateau, PDVTSSe0.325 display the highest slopes for oxidation peak A and reduction peak C. This indicates more complete and faster conversion during battery reactions, contributing to superior reaction kinetics. Additionally, as shown in Figure 4g-i) Tafel slopes derived from the CV data reveal that at full discharging (Peak B) and full charging (peak A), $PDVTSSe_{0.325}$ exhibit the lowest Tafel slope of 0.024 V dec^{-1}, 0.23 V dec^{-1} among the three cathodes, respectively. This suggests faster reaction kinetics during both discharging and charging processes. This performance enhancement can be attributed to the synergistic effect between Se and S, where an optimal Se content accelerates discharge reaction completion and promotes reversible conversion between discharge products and the initial active material.

Understanding the molecular-level orbital changes of cathode materials during battery cycling is essential for elucidating SCP-Li battery performance, stability, and overall lifespan. In this study, the SCP cathodes with and without Se doping are evaluated. Specifically, the initial lithiation processes of three cathodes with different Se contents were analyzed through Gibbs free energy (ΔG) calculations, using dimeric structures to represent the molecular architecture of the SCPs. Due to differences in bond cleavage sites during initial lithiation, the ΔG values vary across different lithiation pathways, which allows for the assessment of lithiation probability based on reaction thermodynamics. A lower Gibbs free energy corresponds to a more spontaneous lithiation reaction[32]. As shown in Figure S9 in Supplementary Information, $PDVTSSe_{0.325}$ does not exhibit the lowest ΔG among the three cathodes, which thermodynamically explains the electrochemical behaviors observed in Figures 4e and 4h. Those results suggest that $PDVTSSe_{0.191}$ and $PDVTSSe_{0.766}$ undergo faster initial lithiation. Notably, the lithiation pathway of $PDVTSSe_{0.325}$ aligns well with the predicted mechanism, as illustrated in Figure 5a. Lithiation initiates via bond cleavage at site-1, yielding the intermediate $LiSSeSC_4H_8S_2SeSLi$ and two equivalents of Li_2S, with a reaction free energy of ΔG = -274 kcal moL^{-1}. Upon further lithiation, the intermediate transforms into $LiSC_4H_8SLi$ and two equivalents of Li_2Se, with ΔG = -173.8 kcal moL^{-1}. These results corroborate the proposed lithiation mechanism and its thermodynamic feasibility, further highlighting the role of Se in modulating the reaction thermodynamics of SCP cathodes. Compared with the undoped PDVTHS cathode (Figure S10 in Supplementary Information), the Se-doped $PDVTSSe_{0.325}$ shows a lower ΔG for lithiation, indicating a more thermodynamically favorable and spontaneous reaction. This suggests that the Se-doped cathode exhibits a faster redox reaction rate and enhanced Li^+ transport, that is consistent with the GITT results.

To visualize the charge distribution, electrostatic potential (ESP) analyses are performed on $PDVTSSe_{0.325}$ and PDVTHS. As shown in Figure 5b, in the $PDVTSSe_{0.325}$ molecule, the blue regions indicate electron-deficient areas are primarily localized around the Se atoms, corresponding to regions of positive electrostatic potential. In contrast, the red regions representing electron-rich areas are mainly concentrated near the S atoms, corresponding to more negative potentials and nucleophilic character[8]. Furthermore, the presence of a continuous negative ESP pathway along the polymer backbone facilitates efficient interchain electron transport. When S and Se form covalent bonds, the higher electronegativity of S causes the electron cloud around Se to shift toward S. Upon cleavage of the S–Se bond, electrons near the Se atom tend to remain around the S atom, increasing the electron density and negative potential at the S site (Figure S11 in Supplementary Information). As shown in Figure 5c, the S–Se bond forms through hybridization between the 3*s* and 3*p* orbitals of S and the 4*s* and 4p orbitals of Se. The introduction of Se alters the molecular orbital energy levels and the band structure of the material. In the simplified model used for band structure analysis (Figure 5d), sp^3 hybridization between S and Se generates both bonding (S–Se) and antibonding (S–Se)*, clearly indicating electron flow from Se to S. Figure 5e and f) schematic the lithiation process of the active material is fundamentally governed by the orbital overlap between molecules. Specifically, the 1s empty orbital of terminal Li interacts with the filled S sp^3 orbital to form a Li–S bond. Se doping modulates the density of states (DOS) of the S sp^3 orbital, shifting the Fermi level (E_f) closer to the center of the S sp^3 state. As a result, the highest occupied molecular orbital (HOMO) moves upward and becomes closer to the lowest unoccupied molecular orbital (LUMO), effectively narrowing the bandgap. Density Functional Theory (DFT) calculations confirm these observations: the bandgap of PDVTHS and $PDVTSSe_{0.325}$ are 4.14 eV and 3.89 eV (Figure 5g), respectively. After initial lithiation, the bandgaps of the resulting products $LiS_2C_4H_8S_3Li$ and $LiSeSC_4H_8S_2SeLi$ decrease further to 2.45 eV and 2.41 eV (Figure 5h), respectively. These results demonstrate that Se doping effectively reduces the bandgap, making the lithiation reaction more thermodynamically favorable and leading to more stable lithiation products.

In Figure 6a), the survey spectra clearly indicate the presence of S, Se, and C in all samples. However, peak intensities vary due to differences in their chemical environments. To better understand the redox behavior during charging/discharging, ex-situ XPS analysis of $PDVTSSe_{0.325}$, pristine $PDVTSSe_{0.325}$ cathode and $PDVTSSe_{0.325}$ cathodes at different states are compared. In Figure 6b), the C 1s spectrum of $PDVTSSe_{0.325}$ shows peaks at 284.2 and 284.8 eV, corresponding to C–S and C–C bonds. For $PDVTSSe_{0.325}$ cathode, the C 1s peak splits, likely due to changes in the carbon bonding environment. Upon discharge, the C–S peak shifts positively by 0.3 eV, attributed to molecular chain breakage that strengthens C–S bonding. Since sulfur is more electronegative than carbon, this causes a reduction in the electron density around C atoms. Conversely, the C–C peak shifts negatively by 0.3 eV due to electron gain during discharge, which lowers the binding energy. Peaks at 287.3 and 291.8 eV originate from residual electrolyte species on the cathode surface. Figure 6c) shows the fine S 2p spectra. The peak at 162.8 eV in $PDVTSSe_{0.325}$ is assigned to Se–S bonds and –SH groups, while the 164.0 eV peak corresponds to S–S and S–C bonds. Compared to the $PDVTSSe_{0.325}$, these peaks in the $PDVTSSe_{0.325}$ cathode shift positively by 0.5 eV, reflecting changes in the carbon bonding environment upon cathode fabrication. For $PDVTSSe_{0.325}$ cathode, when discharging to 1.6 V, the S 2p spectrum shows the emergence of peaks corresponding to S–Li (162.1 eV), $LiSC_4H_8S_2Li$ (163.3 eV), partially reduced lithium polysulfides (Li_2S_x, $2 \leq x \leq 4$) at 168.1 eV, and a small amount of reaction byproduct sulfonates

(S=O) at 169.4 eV. On the contrary, upon recharging to 2.8 V, the –SH group (162.9 eV) reappears, while the discharging products, lithium polysulfides (LiPSs), are reversibly converted back to $PDVTSSe_{0.325}$, leading to a decrease in their concentration. The peaks attributed to S–S and S–C bonds also reemerge and shift positively to 168.8 eV due to electron loss during the charging process. Similarly, the Se 3*d* high-resolution spectra[33] exhibit changes analogous to those of sulfur during cycling (Figure 6d)). When discharged to 1.6 V, peaks at 54.8 and 58.3 eV correspond to Se–S bonds, the other peak at 52.5 eV is assigned to the discharge product Se–Li. Upon recharged to 2.8 V, the Se–Li peak disappears, confirming the reversible redox conversion of $PDVTSSe_{0.325}$. Figures 6e-h) show the morphology of $PDVTSSe_{0.325}$ cathodes at different states. In the pristine, partially discharged, and recharged cathodes, the sulfur-containing polymer is uniformly coated on the carbon fibers, with both sulfur and selenium elements evenly distributed. In contrast, the fully discharged cathode (1.6 V) reveals clearly distinguishable carbon fibers. These observations further confirm the reversible conversion of the active material $PDVTSSe_{0.325}$ during battery operation.

To evaluate the electrochemical performance of a series of PDVTSSe electrodes with varying Se content, the SCP-Li batteries are assembled using different electrodes paired with lithium metal. The theoretical capacities of the SCP materials are calculated based on the polymer and the respective S&Se contents. Detailed information is provided in Table S2 in Supplementary Information. In Figure 7a), from 0.05 to 2 C rate, all three cathodes exhibit stable electrochemical performance. At a low rate of 0.05 C, the specific capacities reach 504.2, 543.4, and 434 mAh g^{-1} for $PDVTSSe_{0.776}$, $PDVTSSe_{0.325}$, and $PDVTSSe_{0.191}$ cathodes, respectively. As the rate increase, the $PDVTSSe_{0.325}$ cathode demonstrate superior rate capability, delivering capacities of 335 mAh g^{-1} at 1 C and 210 mAh g^{-1} at 2 C. In contrast, the $PDVTSSe_{0.776}$ and $PDVTSSe_{0.191}$ cathodes show significantly lower capacities of 208 and 96 mAh g^{-1}, and 154 and 57 mAh g^{-1} at the same rates. When the current rate was reverted to 0.1 C, the capacities recover well to 369 mAh g^{-1} ($PDVTSSe_{0.776}$), 427 mAh g^{-1} ($PDVTSSe_{0.325}$), and 380 mAh g^{-1} ($PDVTSSe_{0.191}$). Long-term cycling performance at 0.2 C is shown in Figure 7b), where the $PDVTSSe_{0.325}$ cathode initially deliver 410 mAh g^{-1} and retain 274 mAh g^{-1} after 220 cycles. Figure 7c-e) present galvanostatic charge-discharge (GCD) curves of the three cathodes at various rates. Compared to $PDVTSSe_{0.776}$ and $PDVTSSe_{0.191}$ cathodes, $PDVTSSe_{0.325}$ exhibit smaller electrochemical polarization and deliver higher capacities at identical rates. Figure 7f) shows the long-term cycling stability of $PDVTSSe_{0.325}$ at 1 C, with an initial capacity of 165 mAh g^{-1}, retaining 117 mAh g^{-1} after 630 cycles, capacity retention of 71%, demonstrating excellent electrochemical stability. Furthermore, in Figure S12 in Supplementary Information electrochemical impedance spectroscopy (EIS) measurements of $PDVTSSe_{0.325}$ cathode show a reduced R_{ct} after 630 times of cycling, indicating that the synergistic interaction between S and Se facilitates faster charge transfer and promotes the battery reaction.

It is noteworthy that the above electrochemical performance metrics are calculated based on the total polymer mass. Capacities calculated based on the S and Se content are presented in the Supporting Information. Therefore, Figure S13 in Supplementary Information compares the rate performance of the three cathodes based on S&Se, showing capacities of 625, 710, and 580 mAh g^{-1} at 0.05 C for $PDVTSSe_{0.776}$, $PDVTSSe_{0.325}$, and, $PDVTSSe_{0.191}$, respectively. Figure S14 and S15 in Supplementary Information show the long-term cycling performance of $PDVTSSe_{0.325}$(initial capacity of 209 mAh g^{-1}) based on S&Se content, and a comparison of capacities for $PDVTSSe_{0.776}$ and $PDVTSSe_{0.191}$ cathodes calculated from polymer mass and S&Se content.

4. Conclusions

In summary, a series of PDVTSSe materials with varying Se contents were synthesized using the previously established thiol–sulfur click chemistry method. Electrochemical and spectroscopic analyses confirmed that $PDVTSSe_{0.325}$ exhibits the best cathodic performance among the synthesized materials. By introducing Se, a group VI element similar to S, S and Se atoms in the $PDVTSSe_{0.325}$ framework undergo sp^3 hybridization to form S−Se covalent bonds. DFT calculations reveal that this structural modification precisely tunes the HOMO energy level and significantly reduces the HOMO/LUMO bandgap (E_g), facilitating the lithiation process and enhancing reaction kinetics. GITT and rate capability tests demonstrate that Se incorporation increases the Li^+ diffusion coefficient to 2.7×10^{-12} cm^2 S^{-1}, an order of magnitude improvement, while also delivering good capacity under high-rate conditions. This study presents a viable strategy of heteroatom (Se) engineering to modulate frontier orbital energies and accelerate battery kinetics, offering a new pathway for the rational design of sulfur-containing conjugated polymers (SCPs).

AUTHOR INFORMATION

Corresponding Authors

Xuejun Ren − *School of Engineering, Liverpool John Moores University, Liverpool L3 3AF, U.K.*; Email: x.j.ren@ljmu.ac.uk

Haifei Zhang − *Department of Chemistry, University of Liverpool, Liverpool L69 7ZD, U.K.*; Email: zhanghf@liverpool.ac.uk

Fen Ran − *Energy Storage Institute of Lanzhou University of Technology, State Key Laboratory of Advanced Processing and Recycling of Non-ferrous Metals, Department of Polymeric Materials Engineering, School of Materials Science and Engineering, Lanzhou University of Technology,Lanzhou 730050 Gansu, China;* orcid.org/0000-0002-7383-1265; Email: ranfen@lut.edu.cn, ranfen@163.com

Authors
Rong Zou – *Energy Storage Institute of Lanzhou University of Technology, State Key Laboratory of Advanced Processing and Recycling of Non-ferrous Metals, Department of Polymeric Materials Engineering, School of Materials Science and Engineering, Lanzhou University of Technology, Lanzhou 730050 Gansu, China; Department of Chemistry, University of Liverpool, Liverpool L69 7ZD, U.K.*
Wenwu Liu – *Energy Storage Institute of Lanzhou University of Technology, State Key Laboratory of Advanced Processing and Recycling of Non-ferrous Metals, Department of Polymeric Materials Engineering, School of Materials Science and Engineering, Lanzhou University of Technology, Lanzhou 730050 Gansu, China*
Binhang Zhao – *Department of Chemistry, University of Liverpool, Liverpool L69 7ZD, U.K.* Jie Zhang – *Energy Storage Institute of Lanzhou University of Technology, State Key Laboratory of Advanced Processing and Recycling of Non-ferrous Metals, Department of Polymeric Materials Engineering, School of Materials Science*
and Engineering, Lanzhou University of Technology, Lanzhou 730050 Gansu, China
Lei Zhao – *Energy Storage Institute of Lanzhou University of Technology, State Key Laboratory of Advanced Processing and Recycling of Non-ferrous Metals, Department of Polymeric Materials Engineering, School of Materials Science and Engineering, Lanzhou University of Technology, Lanzhou 730050 Gansu, China*

Acknowledgments

This work was partly supported by the Regional Project of National Natural Science Foundation (52462034), the Key Talent Project Foundation of Gansu Province, Joint fund between Shenyang National Laboratory for Materials Science and State Key Laboratory of Advanced Processing and Recycling of Nonferrous Metals (18LHPY002), the Incubation Program of Excellent Doctoral Dissertation-Lanzhou University of Technology, the Major Science and Technology Project of Gansu Province (24ZD13GA018, 22ZD6GA008), Science and Technology Program of Gansu Province (22JR5RA240), and the Program for Hongliu Distinguished Young Scholars in Lanzhou University of Technology. *Part of the collaborative work was sponsored by the European Union's Horizon 2020 research and innovation programme under the Marie Skłodowska-Curie grant agreement No:* 101130406 and UKRI Engineering and Physical Sciences Research Council (EP/Y03659X/1). The founders had no role in study design, data collection and analysis, decision to publish, or preparation of the manuscript.

Conflict of Interest

The authors declare no conflict of interest.

Supplemental Information

The Supporting Information is available free of charge at https://pubs.acs.org/doi/10.1021/acs.chemmater.5c02414.

Reference

[1] Pengfei Sang, Qiliang Chen, Dan-Yang Wang, Wei Guo, Yongzhu Fu, Organosulfur materials for rechargeable batteries: Structure, mechanism, and application. *Chemical Reviews* **2023,** *123* (4), 1262-1326.

[2] Zongshuai Gong, Silin Zheng, Jin Zhang, Yueqin Duan, Zhiqiang Luo, Fengshi Cai, Zhihao Yuan, Cross-linked PVA/HNT composite separator enables stable lithium-organic batteries under elevated temperature. *ACS Applied Materials & Interfaces* **2022,** *14* (9), 11474-11482.

[3] Yuki Hanyu, Yoshiyuki Ganbe, Itaru Honma, Application of quinonic cathode compounds for quasi-solid lithium batteries. *Journal of Power Sources* **2013,** *221*, 186-190.

[4] Yanliang Liang, Peng Zhang, Jun Chen, Function-oriented design of conjugated carbonyl compound electrodes for high energy lithium batteries. *J Chemical Science* **2013,** *4* (3), 1330-1337.

[5] Wenfei Wei, Long Li, Lei Zhang, Jianhe Hong, Gang He, An all-solid-state Li-organic battery with quinone-based polymer cathode and composite polymer electrolyte. *Electrochemistry Communications* **2018,** *90*, 21−25.

[6] Rekha Narayan, Aleksandar Blagojevic, Gregor Mali, John Fredy Vélez Santa, Jan Bitenc, Anna Randon-Vitanova, Robert Dominko, Nanostructured poly(hydroquinonyl-benzoquinonyl sulfide)/multiwalled carbon nanotube composite cathodes: improved synthesis and performance for rechargeable Li and Mg organic batteries. *Chemistry of Materials* **2022,** *34* (14), 6378-6388.

[7] Zehao Yu, Liya Huang, Zhe Sun, Fengshi Cai, Mao Liang, Zhiqiang Luo, Designing anthraquinone-based conjugated microporous polymers with dual-ion storage behavior towards high-performance lithium-organic batteries. *Journal of Power Sources* **2022,** *550*, 232149.

[8] Yan Chen, Mingcong Yang, Wei Hu, Tao Chen, Jun Li, Shun Wang, Huile Jin, Jichang Wang, Tailoring the periphery aliphatic group of cathode organosulfide for rechargeable high-performance all-solid-state lithium battery. *Energy & Environmental nvironmental Materials* **2025,** *8* (2), e12819.

[9] Rong Zou, Wenwu Liu, Fen Ran, Sulfur-containing polymer cathode materials: From energy storage mechanism to energy density. *InfoMat* **2022,** *4* (8), e12319.

[10] Dan-Yang Wang, Wei Guo, Yongzhu Fu, Organosulfides: an emerging class of cathode materials for rechargeable lithium batteries. *Accounts of Chemical Research* **2019,** *52* (8), 2290-2300.

[11] Xiuqing Zhang, Wei Guo, Yongzhu Fu, Hybrid organosulfur cathode materials for rechargeable lithium batteries. *Accounts of Materials Research* **2024,** *5* (3), 316-328.

[12] Coralie Jehanno, Jill W Alty, Martijn Roosen, Steven De Meester, Andrew P Dove, Eugene Y-X

Chen, Frank A Leibfarth, Haritz Sardon, Critical advances and future opportunities in upcycling commodity polymers. *Nature* **2022,** *603* (7903), 803-814.
[13] Rong Zou, Wenwu Liu, Fen Ran, Selenium-doped cathode materials with polyaniline skeleton for lithium-organosulfur batteries. *Journal of Energy Chemistry* **2023,** *79* (4), 148-157.
[14] Wei Guo, Dan-yang Wang, Qiliang Chen, Yongzhu Fu, Advances of organosulfur materials for rechargeable metal batteries. *Advanced Science* **2021,** *9* (4), e2103989.
[15] Delyana Marinova, Lyuben Borislavov, Silva Stanchovska, Konstantin Konstantinov, Monika Mutovska, Stanimir Stoyanov, Yulian Zagranyarski, Yanislav Danchovski, Hristo Rasheev, Alia Tadjer, Effect of the peri-annulated dichalcogenide bridge on the bipolar character of naphthalimide derivatives used as organic electrode materials. *Materials Letters* **2025,** *18* (9), 2066.
[16] Zhenzhen Wu, Qirong Liu, Pan Yang, Hao Chen, Qichun Zhang, Sheng Li, Yongbing Tang, Shanqing Zhang, Molecular and morphological engineering of organic electrode materials for electrochemical energy storage. *Electrochemical Energy Reviews* **2022,** *5* (Suppl 1), 26.
[17] Yang Zhao, Zuhao Quan, Nuo Xu, Hongtao Zhang, Yongsheng Chen, MoS2-modified N-doped graphene/organosulfide composite cathode material for high-performance lithium–sulfur Batteries. *ACS Applied Energy Materials* **2025,** *8* (4), 2360-2368.
[18] Rong Zou, Wenwu Liu, Fen Ran, A new thiol-sulfur click chemistry for lithium-organosulfide batteries. *the Innovation* **2025,** *6* (2), 100765.
[19] Frank Neese, Software update: The ORCA program system—Version 5.0. *WIREs Computational Molecular Science* **2022,** *12* (5), e1606.
[20] Florian Weigend, Reinhart Ahlrichs, Balanced basis sets of split valence, triple zeta valence and quadruple zeta valence quality for H to Rn: Design and assessment of accuracy. *Physical Chemistry Chemical Physics* **2005,** *7* (18), 3297-3305.
[21] Tian Lu, Qinxue Chen, Shermo: A general code for calculating molecular thermochemistry properties. *Computational Theoretical Chemistry Accounts* **2021,** *1200*, 113249.
[22] Joost VandeVondele, Jürg Hutter, Gaussian basis sets for accurate calculations on molecular systems in gas and condensed phases. *The Journal of Chemical Physics* **2007,** *127* (11).
[23] W. Humphrey, A. Dalke, K. Schulten, VMD: Visual molecular dynamics. *Journal of Molecular Graphics & Modelling* **1996,** *14* (1), 33-38.
[24] Wei Li, Yongsong Ma, Peng Li, Xiaoyun Jing, Kai Jiang, Dihua Wang, Synergistic Effect between S and Se Enhancing the Electrochemical Behavior of SexSy in Aqueous Zn Metal Batteries. *Advanced Functional Materials* **2021,** *31* (20), 2101237.
[25] Yunyang Zhang, Yulong Sun, Linfeng Peng, Jiaqiang Yang, Huanhuan Jia, Zhuoran Zhang, Bin Shan, Jia Xie, Se as eutectic accelerator in sulfurized polyacrylonitrile for high performance all-solid-

state lithium-sulfur battery. *Energy Storage Materials* **2019,** *21*, 287-296.
[26] Longtao Ren, Lu Qiao, Abdul Hameed Pato, Jun Liu, Yan Wang, Xiwen Lu, Yajun Zhao, Qian Wang, Wen Liu, Haijun Xu, Xiaoming Sun, Suppression of long-chain lithium polysulfide formation through a selenium-doped linear sulfur copolymer cathode for high-performance lithium–organosulfur batteries. *Journal of Materials Chemistry A* **2024,** *12* (7), 4249-4257.
[27] Hao-Jie Li, Kai Xi, Wei Wang, Sheng Liu, Guo-Ran Li, Xue-Ping Gao, Quantitatively regulating defects of 2D tungsten selenide to enhance catalytic ability for polysulfide conversion in a lithium sulfur battery. *Energy Storage Materials* **2022,** *45*, 1229-1237.
[28] Meimei Yu, Yuanyou Peng, Yu Wang, Facai Guo, Fen Ran, All-in-one membrane micro-supercapacitors for implantable devices. *Journal of Membrane Science* **2023,** *687*, 122084.
[29] Yunsik Ohm, Chengfeng Pan, Michael J Ford, Xiaonan Huang, Jiahe Liao, Carmel Majidi, An electrically conductive silver–polyacrylamide–alginate hydrogel composite for soft electronics. *Nature Electronics* **2021,** *4* (3), 185-192.
[30] Tingting Ye, Jiacheng Wang, Yiding Jiao, Luhe Li, Er He, Lie Wang, Yiran Li, Yanjing Yun, Dan Li, Jiang Lu, A tissue-like soft all-hydrogel battery. *Advanced Materials* **2022,** *34* (4), 2105120.
[31] E Samson, J Marchand, Kenneth A Snyder, structures, Calculation of ionic diffusion coefficients on the basis of migration test results. *Materials and structure* **2003,** *36* (3), 156-165.
[32] Lingli Huang, Thuc Hue Ly, Intrinsic defects unlock the growth of rhombohedral stacking. *Nature Materials* **2025**.
[33] Tae Hwa Hong, Woosik Min, Gwanghyeon Choi, Jea Duk Kim, Jung Tae Lee, Duho Kim, Unified Interplay of Chemical Bond and Solid-State Kinetics in Lithium–Sulfur Batteries. *Advanced Energy Materials* **2023,** *13* (25), 2300636.

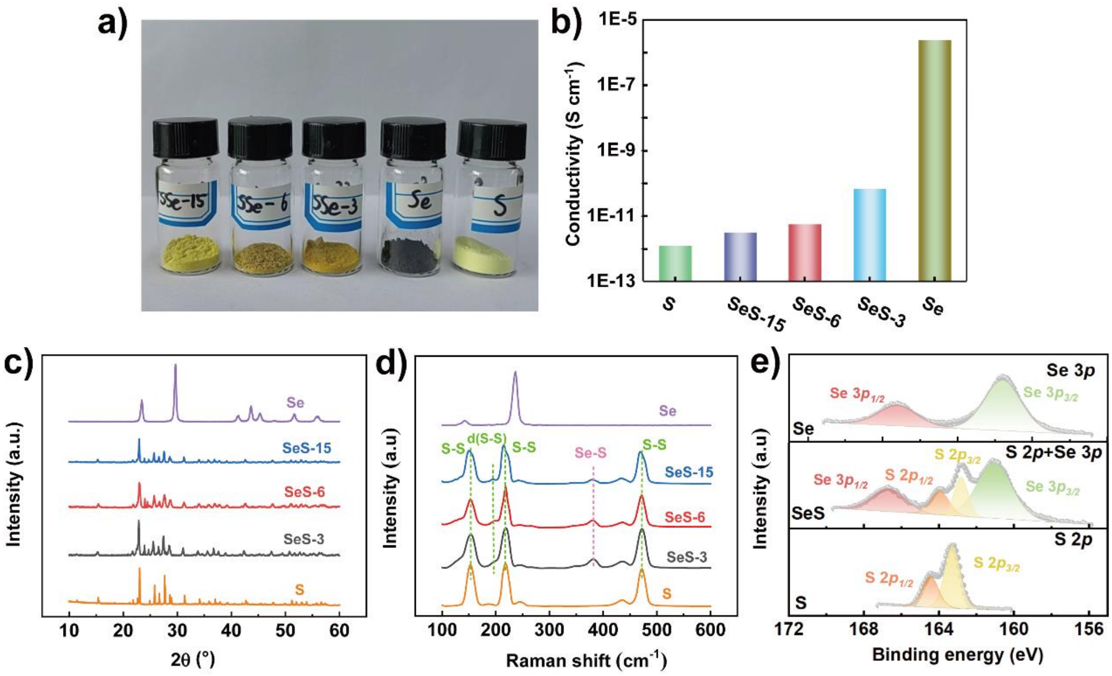

Figure 1. a) Optical photography, b) electronic conductivity, c) XRD patterns and d) Raman patterns of various SeS solid solutions. e) High resolution XPS spectra of Se 3p in pure Se, S 2p + Se 3p in SeS and S 2p in pure S.

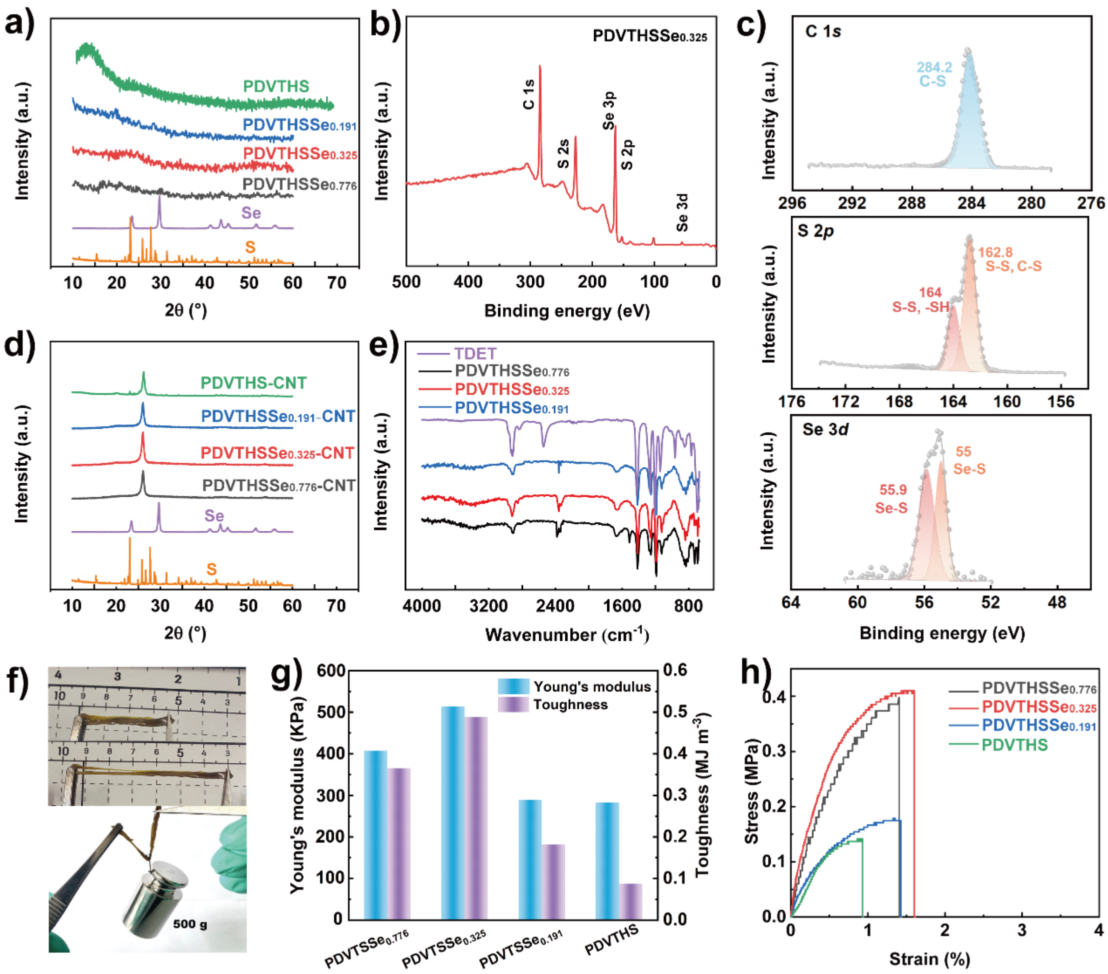

Figure 2. a) XRD patterns of different SCP samples. b) XPS survey spectrum and c) C 1s, S 2p, Se 3d XPS fine spectrum of $PDVTSSe_{0.325}$. d) XRD spectra and e) FTIR of different samples. f) Tensile test digital photograph of $PDVTSSe_{0.325}$. g) Toughness and Young's modulus changes curves. h) Stress-strain curves of different samples.

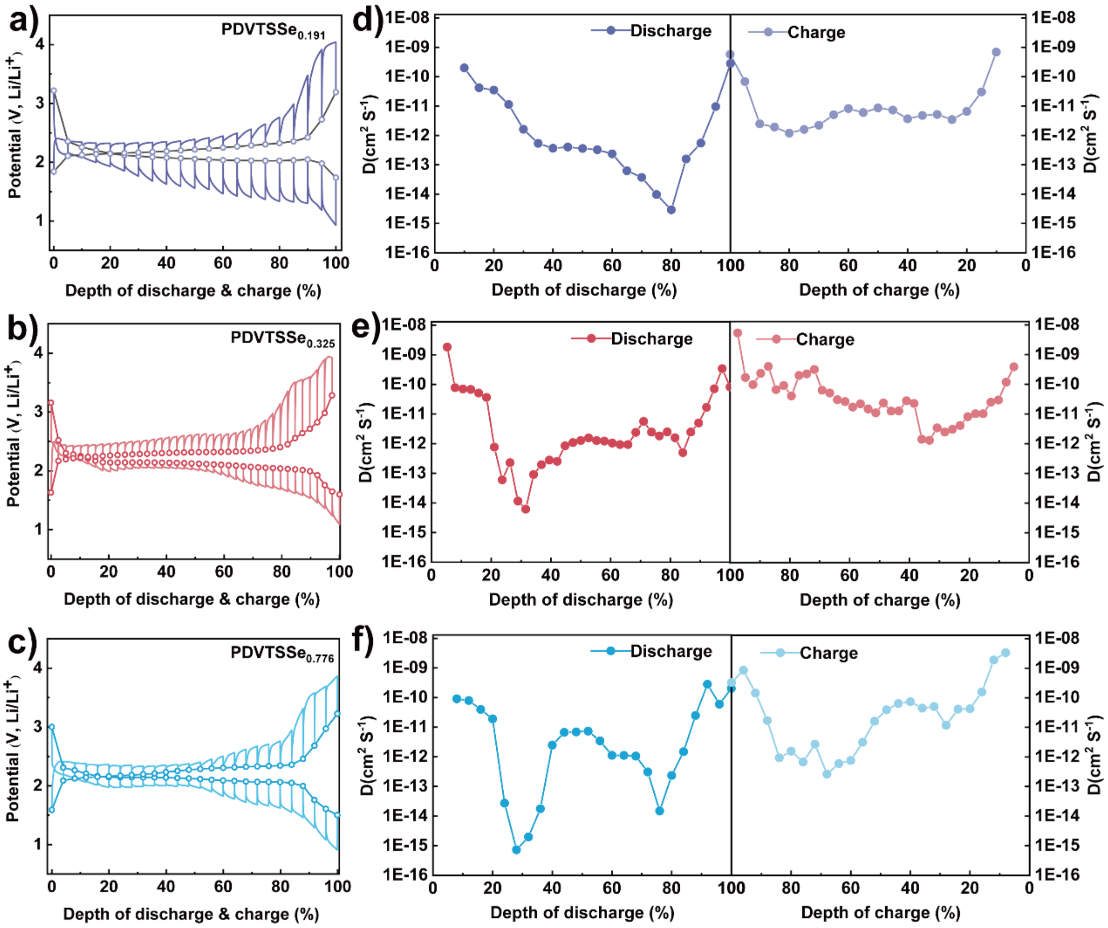

Figure 3. a-c) GITT curves of the variants with different Se content, and corresponding Li^+ diffusion coefficients in d) PDVTSSe$_{0.191}$, e) PDVTSSe$_{0.325}$, and f) PDVTSSe$_{0.776}$.

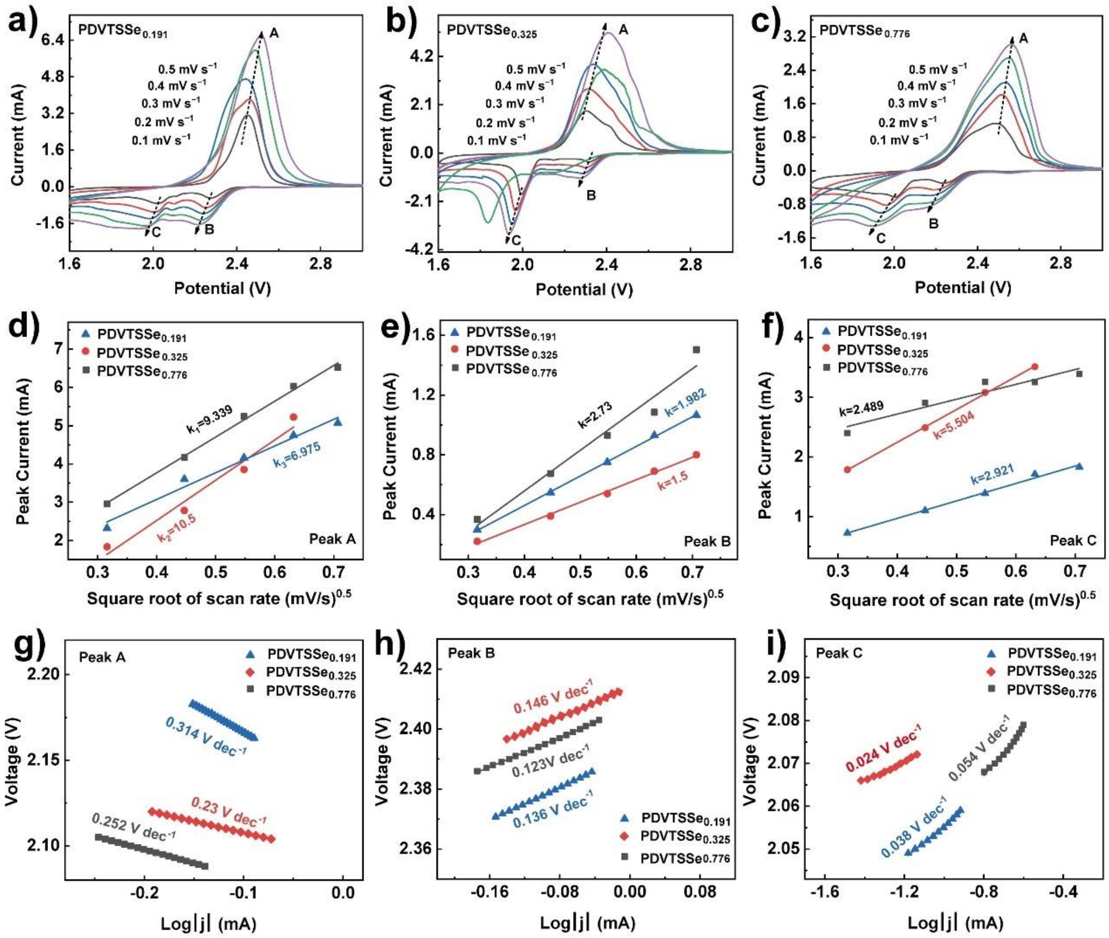

Figure 4. CV curves of a) $PDVTSSe_{0.191}$, b) $PDVTSSe_{0.325}$, and c) $PDVTSSe_{0.776}$ at different scan rates; d-e) CV redox peaks current vs the square root of scan rate, g-i) Tafle plots of $PDVTSSe_{0.191}$, $PDVTSSe_{0.325}$, and $PDVTSSe_{0.776}$.

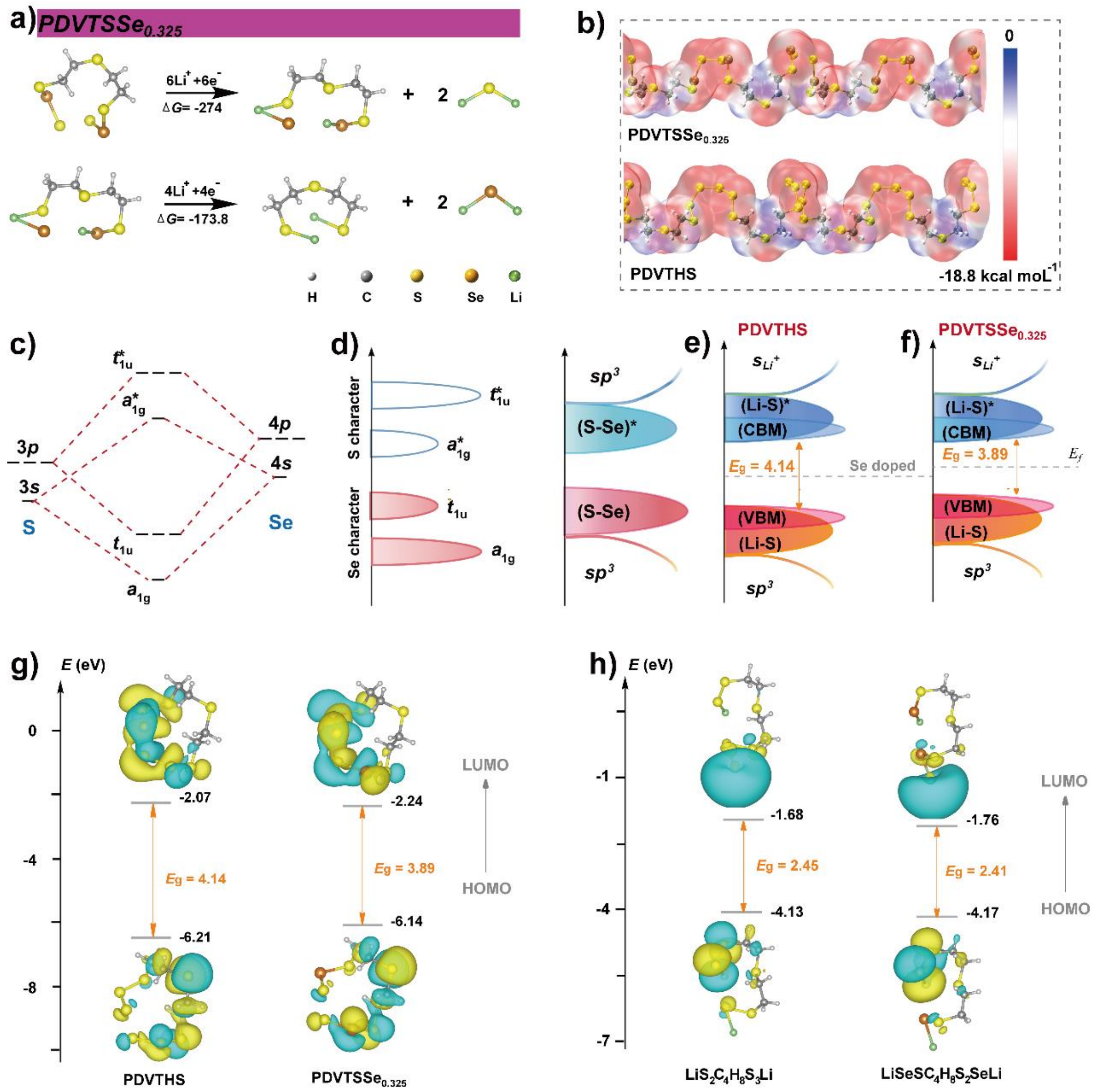

Figure 5. a) The reaction mechanism of $PDVTSSe_{0.325}$ during discharging process and corresponding ΔG. b) Polymer structure and electrostatic potential comparison of $PDVTSSe_{0.325}$ and PDVTSSe. As depicted from c) to d) the schematic band structure of S–Se can be built by extrapolating c) the molecular orbital energy diagram of S and Se. The molecular orbital energy diagram during lithiation for e) PDVTSSe and f) $PDVTSSe_{0.325}$. A comparison of the DFT calculated HOMO/LUMO energy level diagrams of g) PDVTSSe, $PDVTSSe_{0.325}$ and h) single lithiated PDVTHS ($LiS_2C_4H_8S_3Li$), $PDVTSSe_{0.325}$ ($LiSeS\ C_4H_8S_2SeLi$) by frontier molecular orbital analysis.

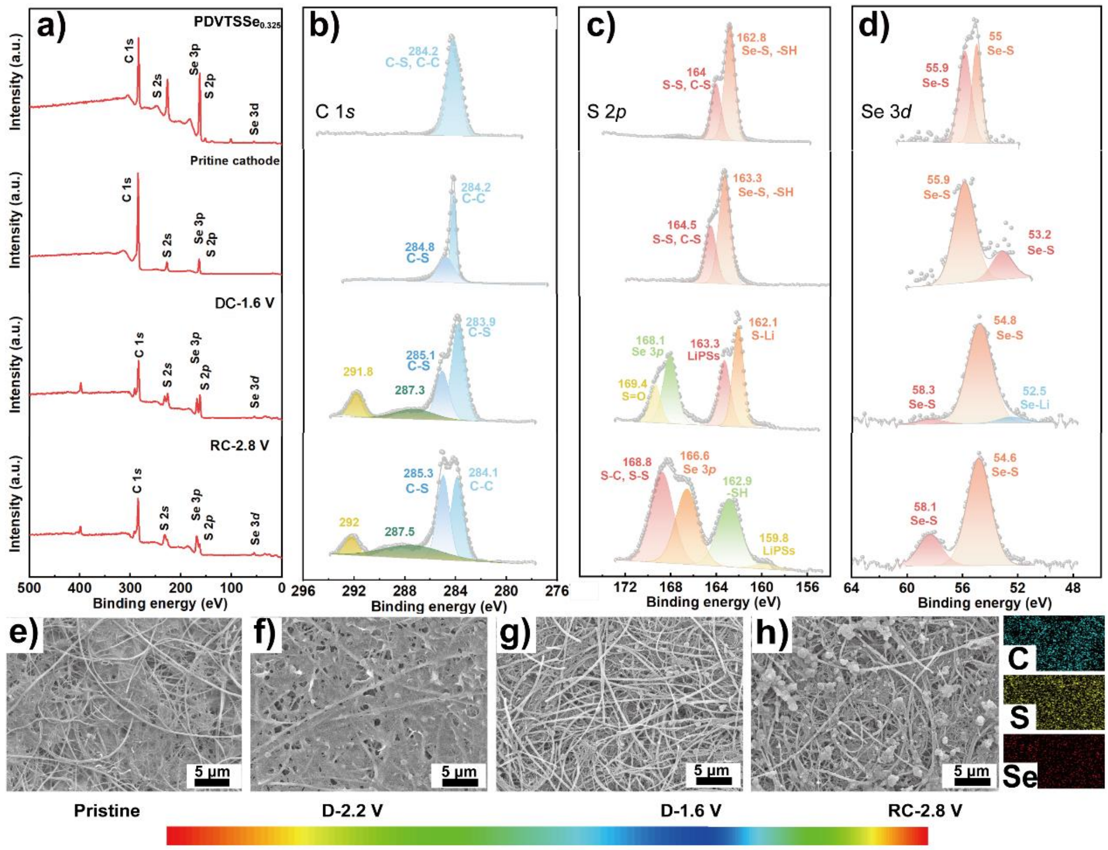

Figure 6. a) XPS spectra of $PDVTSSe_{0.325}$ cathode at different electrochemical states, along with high-resolution spectra of b) C 1s, c) S 2p, and d) Se 3d. e-h) SEM images and corresponding elemental mappings of the fresh $PDVTSSe_{0.325}$ cathode at various charging/discharging states.

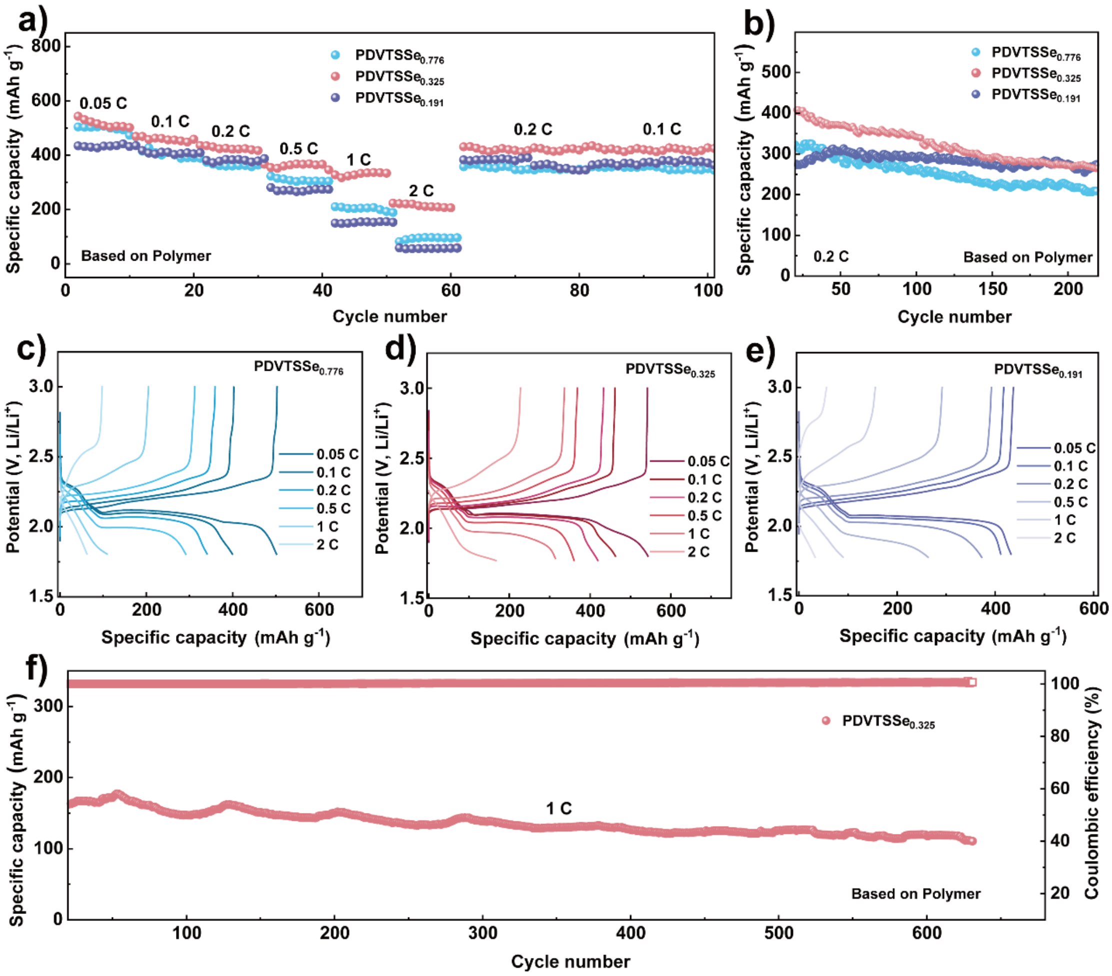

Figure 7. a) Rate properties curves ranging from 0.05 to 2 C, b) cycling performance at 0.2 C and c-e) the corresponding GCD curves for different cathodes; f) Long-term cycling performance of $PDVTSSe_{0.325}$ cathode at 1 C.